

# The Distance to Clusters: Correcting for Asphericity

David C. Fox

*Physics Department, Harvard University, Jefferson Physical Laboratories, Cambridge, MA 02138*

[davidcfox@post.harvard.edu](mailto:davidcfox@post.harvard.edu)

and

Ue-Li Pen

*Canadian Institute for Theoretical Astrophysics, University of Toronto, McLennan Labs, 60 St. George Street, Toronto, ON, M5S 3H8, Canada*

[pen@cita.utoronto.ca](mailto:pen@cita.utoronto.ca)

## ABSTRACT

X-ray and Sunyaev-Zel'dovich effect observations can be combined to measure the distance to clusters of galaxies. The Hubble constant,  $H_0$ , can be inferred from the distance to low-redshift clusters. With enough clusters to measure the redshift-distance relation out to a redshift  $z \sim 1$ , it may be possible to determine the total matter density,  $\Omega_0$ , and the cosmological constant,  $\Lambda_0$ , as well. If the intracluster gas distribution is not spherical, but elongated by a factor of  $Z$  along the line of sight, the inferred distance is increased by  $Z$ , and  $H_0$  is decreased by the same factor. Averaging the inferred value of  $H_0$  over a sufficiently large sample of clusters can reduce any systematic bias due to cluster shapes, provided the clusters are selected without any preferred orientation. Even so, elongation contributes significantly to the variance in the measured distances and in the inferred value of  $H_0$ .

With the addition of gravitational lensing observations, it is possible to infer the three-dimensional shape of an individual cluster, provided the gas is in hydrostatic equilibrium. We demonstrate a specific method for finding the shape and correcting the measured distances to individual clusters. To test this method, we apply it to artificial observations of simple model clusters. We base the artificial X-ray observations on the Chandra X-ray Observatory. For the SZ effect, we assume modest improvements over current observations at the Owens Valley Radio Observatory. We recover the true distances to each of our clusters without detectable bias, and with statistical errors due to measurement uncertainties of 4 to 6%.

*Subject headings:* cosmic microwave background — distance scale — galaxies: clusters : general — gravitational lensing — X-rays: galaxies: clusters

## 1. Introduction

The discovery of X-ray emission from clusters of galaxies revealed that clusters are filled with ionized gas. Not long after this discovery, Sunyaev & Zel'dovich (1972) pointed out that the electrons in this gas should also scatter photons from the Cosmic Microwave Background (CMB), and that the thermal motion of the electrons would produce a detectable shift in the CMB spectrum. This shift is known as the Sunyaev-Zel'dovich (SZ) effect. Together, SZ effect and X-ray observations of the intracluster gas determine the physical size of the cluster along the line of sight. Comparing this scale with the apparent angular size of the cluster yields a direct measurement of the angular diameter distance, assuming the cluster is spherical (Cavaliere, Danese, & de Zotti 1977; Gunn 1978; Silk & White 1978). This geometric estimate is independent of the usual distance ladder. Using cluster distance and redshift measurements for low redshift clusters, the Hubble constant,  $H_0$ , can be determined. Measurements of the redshift-distance relation at redshifts up to  $z \sim 1$  would constrain the matter density,  $\Omega_0$ , and the cosmological constant,  $\Lambda_0$ , in units of the critical density (Carlstrom et al. 2001).

We know from X-ray images that clusters are often not round in projection, and therefore cannot be spherical (see, e.g., Mohr et al. 1995). A number of authors have investigated the effect of asphericity on the inferred value of  $H_0$ , either with simulations (Inagaki, Sugino, & Suto 1995; Roettiger, Stone, & Mushotzky 1997; Yoshikawa, Itoh, & Suto 1998) or analytic ellipsoidal models of the gas (Cooray 1998, 2000; Hughes & Birkinshaw 1998; Sulkanen 1999; Puy et al. 2000). For an individual cluster, the estimated distance will differ from the actual distance by a factor of the ratio,  $Z$ , of the size of the cluster along the line of sight to its size in the plane of the sky. The usual solution to this problem has been to suggest averaging the inferred values of the Hubble constant over a sample of clusters. Here, we propose a different approach. We will demonstrate that it is possible to infer the three-dimensional shape of an individual cluster, and recover the true distance.

In its simplest form, the idea behind the distance determination is as follows. The SZ effect is caused by Thompson scattering of CMB photons by electrons. It is therefore proportional to the column density,  $N_e = n_e \Delta l$ , where  $n_e$  is the electron number density and  $\Delta l$  is a measure of the path length of a given line of sight through the cluster. The X-ray emission is due to Bremsstrahlung from electron-ion collisions, so the X-ray surface brightness,  $\Sigma_X$ , is proportional to  $n_e^2 \Delta l$ . Squaring  $n_e \Delta l$  and dividing by  $n_e^2 \Delta l$  from the X-

ray observations, we can eliminate the electron density to find the path length. Finally, by comparing this path length with the angular extent of the cluster, we can infer the angular diameter distance,  $D$ , to the cluster. For clusters at redshift  $z \ll 1$ , we can calculate the Hubble constant,  $H_0 = cz/D$ .

We have neglected the fact that both the SZ effect and the X-ray emissivity depend on the temperature of the electrons as well as their density. We describe the method in more detail, taking temperature into account, in §2. However, this simplified picture suffices to illustrate the effect of cluster shapes on the inferred distance. The method assumes that the cluster is spherical, so that the path length along the line of sight and the width of the cluster perpendicular to the line of sight are the same. If the actual gas distribution is not spherical, this assumption can introduce a systematic error in the inferred distance. If the gas distribution is elongated by a factor of  $Z$  along the line of sight, this will increase the measured SZ effect and X-ray surface brightness by  $Z$ , without changing the apparent angular size of the cluster. As a result, the inferred distance will be increased by a factor of  $Z$  relative to the true distance, and  $H_0 = cz/D$  will be underestimated by  $Z$ .

It has generally been assumed that averaging the inferred values of the Hubble constant over different cluster orientations at random would eliminate any systematic bias. In fact, the validity of this assumption seems to depend on both the intrinsic shapes of clusters (whether prolate, oblate or triaxial) and on the choice of projected axis used to establish the angular scale (Cooray 1998, 2000; Sulkanen 1999), though the remaining systematic errors are relatively small (3 — 10%) if the semi-major projected axis is used.

In addition, removing the systematic effect of elongation requires averaging over an unbiased sample of clusters. If clusters are chosen based on X-ray surface brightness or SZ effect amplitude (or eliminated based on non-detections), clusters elongated along the line of sight will be favored (Birkinshaw, Hughes, & Arnaud 1991). Clusters elongated due to recent mergers may be favored because of their higher X-ray luminosity (Roettiger et al. 1997). Some authors (Roettiger et al. 1997) have suggested selecting clusters without evidence of recent mergers, but even this may introduce its own bias if the merger signatures used are not independent of orientation.

Finally, even with an unbiased sample, asphericity contributes roughly 15% to the rms scatter in the value of  $H_0$  from individual clusters (Inagaki et al. 1995; Roettiger et al. 1997; Sulkanen 1999). Thus measurements are required for a large ( $\sim 25$ ) cluster sample. This may limit more detailed studies of the redshift-distance relation to estimate  $\Omega_0$  and  $\Lambda_0$ . Some evidence (Cooray 1998) suggests that a large part of the scatter in measurements of  $H_0$  from X-ray and SZ effect observations is due to variations in cluster shapes.

If we had a method of determining the three-dimensional shape of individual clusters, we could correct for the effect of elongation on the distance. This would enable us to reduce the scatter in the inferred redshift-distance relation. In addition to reducing the number of clusters needed to achieve a given level of precision, this might also allow us to study other effects (to quantify any variations in the clumpiness of the intracluster gas from one cluster to another, for instance).

The degeneracy between the distance,  $D$ , and the elongation factor,  $Z$ , is intrinsic to observations of projected cluster properties. Therefore, to measure elongation without prior knowledge of  $D$ , we need an additional theoretical constraint. An obvious choice is hydrostatic equilibrium. This assumption in turn introduces a new unknown, the cluster mass distribution. To compensate, we must add an additional observational constraint, the projected mass distribution as measured by gravitational lensing. We will prove that the assumption of hydrostatic equilibrium, together with lensing observations, is sufficient to break the degeneracy and allow us to recover both the elongation and the distance.

Such an approach has been suggested by Zaroubi et al. (1998, 2001). Reblinsky (2000) has also discussed a method for reconstruction of the three-dimensional structure of clusters. The perturbative approach of Dore et al. (2001) may also be useful in inferring asphericity. Cooray (1998) has suggested a somewhat different way of breaking the same degeneracy. While it also combines X-ray, SZ effect, and lensing observations, it is based on the assumption of a universal (and measurable) baryon fraction for clusters, rather than on that of hydrostatic equilibrium.

We will demonstrate that our method can successfully recover the shape and distance with high accuracy when applied to simple analytical models of clusters. We first test the method on clusters which are axisymmetric about line of sight, and then on triaxial clusters of arbitrary orientation. In the future, we will test its ability to do the same when applied to simulated clusters, which more closely resemble real ones, at least in their complexity and asymmetry. We should note that one advantage of the traditional method of inferring  $H_0$  from SZ effect and X-ray observations is that it does not depend on hydrostatic equilibrium. Deviations from hydrostatic equilibrium in real clusters may introduce a systematic error in the value of  $H_0$  inferred from any method which does rely on this assumption. It is essential to apply our method to simulated clusters to attempt to quantify any such systematic error.

In §2, we will explain the elongation-distance degeneracy in more detail. By using ellipsoidal potentials, we will prove analytically that the hydrostatic equilibrium assumption and weak lensing observations are sufficient in principle to break the degeneracy in the case of a cluster axisymmetric about the line of sight. In practice, the actual model we use to infer the elongation from artificial observations uses ellipsoidal mass distributions. We will

formulate this method in §3 for clusters with arbitrary triaxial shapes.

In §4, we will introduce the simple analytic clusters we use to test the de-projection method. We will describe how we construct artificial observations of these clusters, and specify our assumptions about the uncertainties in these observations in §5. Some additional numerical details of the calculation are described in §6. We apply our de-projection method to these clusters and present our results in §7. We discuss the uncertainties in the inferred distance, both statistical and systematic in §8. Finally, in §9, we will summarize our conclusions and highlight directions for future work.

## 2. The Elongation-Distance Degeneracy

### 2.1. The Spherical Case

To understand how the distance can be determined from X-ray and SZ effect measurements, consider the observables. The Sunyaev-Zel'dovich effect is due to the Compton scattering of microwave background photons by the electrons in the intracluster plasma, with a probability per unit path length,  $dl$ , equal to the Thomson cross-section,  $\sigma_T$ , times the electron density,  $n_e$ . The photon frequency,  $\nu$ , follows a random walk with  $(\delta\nu/\nu)^2$  per scattering equal to the line of sight velocity dispersion  $\langle v_{LOS}^2 \rangle = kT_e/m_e$  of the electrons, divided by  $c^2$ . The variance  $(\delta\nu/\nu)^2$  integrated along the path through the cluster is given by the Compton  $y$ -parameter,

$$y \equiv \left( \frac{\delta\nu}{\nu} \right)^2 = \frac{k\sigma_T}{m_e c^2} \int dl n_e T_e, \quad (1)$$

where  $k$  is Boltzmann's constant. Observationally, what is measured is not the frequency shift of individual photons, but the change in the black body spectrum of the CMB. This is commonly expressed in terms of the shift in the brightness temperature at a given frequency,  $(\Delta T/T)_{\text{CMB}}(\nu)$ , which is proportional to  $y$ :

$$\left( \frac{\Delta T}{T} \right)_{\text{CMB}}(\nu) = f(h\nu/kT_{\text{CMB}}, T_e) y, \quad (2)$$

where  $f \approx -2$  (plus relativistic corrections) when  $h\nu/kT_{\text{CMB}} < 1$ . When we refer to the SZ effect, we mean, technically, the thermal SZ effect due to the isotropic, thermal motions of the electrons. If the cluster has a nonzero peculiar velocity with respect to the Hubble flow, this will cause a systematic frequency shift known as the kinetic SZ effect.

The X-ray emissivity is due to Bremsstrahlung from electron-ion collisions, so it is proportional to the square of the electron density. Modern X-ray telescopes, such as the

Chandra X-ray Observatory (Chandra) and XMM-Newton, can measure the X-ray surface brightness as a function of photon energy, with spectral resolving power  $E/\Delta E \sim 20 - 40$  at 6 keV. Thus, they can measure the X-ray surface brightness per unit energy interval,

$$\frac{d\Sigma_X}{dE} = \frac{1}{4\pi(1+z)^3} \int dl n_e^2 \frac{d\Lambda(T_e, E')}{dE'}, \quad (3)$$

where  $z$  is the redshift of the cluster,  $E$  is the photon energy in the observer's frame,  $E' \equiv E(1+z)$  is the rest frame photon energy, and  $d\Lambda(T_e, E')/dE'$  is the X-ray spectral emissivity.

Both the X-ray surface brightness and the temperature decrement can be mapped as a function of angular position,  $\theta$ , on the sky. If the electron density and temperature are spherically symmetric, then these spatially resolved observations can be de-projected. Because the observations are functions of angular position,  $\theta$ , the de-projection determines  $Dn_e T_e$  and  $Dn_e^2 d\Lambda(T_e, E')/dE'$  as functions of  $r/D$ , where  $r$  is the radius and  $D$  is the angular diameter distance to the cluster. Given X-ray observations with sufficient spatial and energy resolution, the temperature profile,  $T_e(r/D)$ , can be inferred. This allows us to eliminate the temperature-dependent factors, to obtain  $Dn_e$  from  $(\Delta T/T)_{\text{CMB}}$  and  $Dn_e^2$  from  $\Sigma_X$ . The ratio of the square of the SZ effect measurement to the X-ray measurement gives the angular diameter distance.

## 2.2. The Elongation-Distance Degeneracy

Now, suppose that contours of constant  $n_e$  and  $T_e$  are not spherical, but are instead elongated by a factor of  $Z$  along the line of sight. Then, the integration path length and thus the normalization of the projected observables will be increased by a constant factor of  $Z$ . The shapes of the measured profiles,  $(\Delta T/T)_{\text{CMB}}(\theta)$  and  $\Sigma_X(\theta)$  will be unchanged, so there will be no obvious sign that the cluster is not spherical. If the data are analyzed under the assumption of spherical symmetry, the inferred distance will be  $DZ^2/Z = DZ$ , since the square of the temperature decrement is being compared to the X-ray surface brightness.

Any method which relies on the normalization of quantities integrated along line of sight suffers from this degeneracy; only the product of the distance and the elongation can be determined. Observations of additional projected quantities do not help. The only way to break the degeneracy is to postulate an additional constraint among the cluster properties. The hydrostatic equilibrium condition,

$$\nabla p = -\rho_{\text{gas}} \nabla \phi, \quad (4)$$

provides such a constraint between the pressure,  $p$ , the gas density,  $\rho_{\text{gas}}$ , and the gravitational potential,  $\phi$ .

Of course, while hydrostatic equilibrium adds a constraint, it also introduces a new unknown, the gravitational potential,  $\phi$ , of the cluster. Fortunately, this extra degree of freedom can in turn be constrained by weak gravitational lensing observations, as we will see in §2.3. Then, in §2.4, we will show how adding weak lensing data and the hydrostatic equilibrium condition allows us to break the degeneracy.

### 2.3. Gravitational Lensing

The gravitational potential of a cluster deflects light rays from sources behind the cluster. The lensing effect is determined by the convergence,  $\kappa$ , which is the ratio of the projected surface density,  $\Sigma(\boldsymbol{\theta})$ , of the lens at angular position  $\boldsymbol{\theta}$ , to the critical surface density,

$$\Sigma_{\text{cr}} \equiv \frac{c^2}{4\pi G} \frac{D_s}{D_l D_{ls}}, \quad (5)$$

where  $D_s$ ,  $D_l$ , and  $D_{ls}$  are angular diameter distances to the source, to the lens, and from the lens to the source, respectively. Since each of the angular diameter distances is proportional to  $H_0^{-1}$ ,  $\Sigma_{\text{cr}}$  is proportional to  $H_0$ . However, the product  $D_l \Sigma_{\text{cr}}$  which we will encounter depends only on the source and lens redshifts, and on the cosmological parameters ( $\Omega_0$ ,  $\Lambda_0$ , etc.) which determine the shape of the redshift-distance relation, but is independent of  $H_0$ .

The convergence is also equal to  $(1/2)\nabla^2\psi$ , where

$$\psi(\boldsymbol{\theta}) = \frac{1}{2\pi G \Sigma_{\text{cr}} D_l^2} \int dl \phi, \quad (6)$$

is called the lens potential (Schneider, Ehlers, & Falco 1992).

The deflection of light rays distorts the images of background galaxies, magnifying them in both area and flux, and changing their shapes. In the weak lensing limit, where the second partial derivatives  $|\psi_{,ij}| \ll 1$ , these effects must be measured statistically by averaging over many background galaxies. In this limit, the images are magnified by  $1 + 2\kappa$ , while the distortion in their shapes is characterized by the 2-component shear,  $\gamma_i$ , where

$$\gamma_1 = \frac{1}{2}(\psi_{,11} - \psi_{,22}) \quad (7)$$

and

$$\gamma_2 = \psi_{,12}. \quad (8)$$

Direct measurements of the magnification in the weak lensing limit are difficult, though several techniques have been suggested (Bartelmann & Narayan 1995; Broadhurst, Taylor,

& Peacock 1995) and at least one cluster has been detected and mapped by such techniques (Taylor et al. 1998). More frequently, the shear is measured from the galaxies shapes. Kaiser & Squires (1993) demonstrated a method for reconstructing  $\kappa$ , up to a constant offset, from maps of the shear (see Mellier 1999, for a review). The ambiguity of this offset is known as the mass sheet degeneracy.

We should note that equation (5) assumes a single, known source redshift,  $z_s$ . In the weak lensing limit,  $\Sigma_{\text{cr}}^{-1}$  can simply be replaced with its average over the redshifts of the sources (Kaiser & Squires 1993; Seitz & Schneider 1997). Still, it is necessary to estimate the source redshift distribution. For  $z_l \ll z_s$ , this task is simplified by the fact that the ratio  $D_s/D_{ls}$  becomes independent of the source redshift. More generally, several methods have been suggested for estimating the source redshift distribution from the lensing data itself (Smail, Ellis, & Fitchett 1994; Kneib et al. 1994, 1996; Bartelmann & Narayan 1995).

## 2.4. Breaking the Degeneracy

Equation (4) implies that the contours of constant pressure coincide with the cluster isopotentials. Taking the curl of both sides, we see that  $\nabla \rho_{\text{gas}} \times \nabla \phi = 0$ , so the isopotentials are also contours of constant gas density. Finally, since  $p = \rho_{\text{gas}} kT / \mu m_p$ , where  $\mu m_p$  is the mean mass per particle, they are contours of constant temperature as well. Thus, for a potential with a single minimum, both  $\rho_{\text{gas}}$  and  $T$  are functions of  $\phi$ . Then, the balance between pressure and gravity perpendicular to the isopotentials can be rewritten as

$$\frac{dp}{d\phi} = -\rho_{\text{gas}}, \quad (9)$$

or

$$\frac{dT}{d\phi} + T \frac{d \log n_e}{d\phi} = -\frac{\mu m_p}{k}. \quad (10)$$

Since the observations are made as a function of angular position,  $\boldsymbol{\theta}$ , it is convenient to define a coordinate  $\zeta = l/D$ . Then, we can define a three-dimensional position  $\mathbf{x} \equiv \mathbf{r}/D = (\boldsymbol{\theta}, \zeta)$  in radians. We also define the ellipsoidal equivalent,  $m$ , of a radius, by

$$m^2 \equiv \mathbf{x} \cdot E^2 \cdot \mathbf{x}, \quad (11)$$

where  $E^2$  is a symmetric, positive-definite matrix. Surfaces of constant  $m$  form a family of similar, concentric, coaxial ellipsoids. In the case of a cluster with isopotentials elongated along the line of sight by  $Z$ ,

$$m = \sqrt{\boldsymbol{\theta}^2 + \zeta^2/Z^2}. \quad (12)$$

The gas properties are functions of  $\phi$  and thus of  $m$ .

If we apply a spherical de-projection to such an elongated cluster, we will obtain  $DZn_eT_e$  and  $DZn_e^2 d\Lambda(T_e, E')/dE'$  as functions of  $m$ . Again, we can extract the temperature profile,  $T_e(m)$ , which depends only on the ratio between the X-ray surface brightness in different bands, and is therefore independent of  $Z$ . Rewriting equation (10) in terms of derivatives with respect to  $m$ , we see that

$$\frac{dT}{dm} + T \frac{d \log n_e}{dm} = - \frac{\mu m_p}{k} \frac{d\phi}{dm}. \quad (13)$$

Both terms on the left-hand side of this equation can be inferred from the X-ray observations, independent of  $D$  and  $Z$ , so we can integrate to find  $\phi(m)$  independent of  $D$  or  $Z$ . Equation (6) relates  $\phi$  to  $\psi$ , so we can predict

$$\int d\zeta \phi(m(\boldsymbol{\theta}, \zeta)) = \frac{1}{Z} \int d(l/D_l) \phi = \frac{2\pi G \Sigma_{\text{cr}} D_l}{Z} \psi(\boldsymbol{\theta}) \quad (14)$$

as a function of  $\boldsymbol{\theta}$ . As we noted in §2.3,  $\Sigma_{\text{cr}} D_l$  depends upon the source and lens redshifts and on cosmology, but is independent of  $D_l$  and  $H_0$ , so we can predict  $\psi/Z$ . Taking the appropriate partial derivatives with respect to  $\theta_i$ , we can calculate both  $\kappa/Z$  and  $\gamma/Z$ . Comparing with  $\kappa$  or  $\gamma$  from lensing observations, we can solve for the elongation,  $Z$ . Either  $\kappa$  or  $\gamma$  is sufficient to fix  $Z$ . Therefore, in principle,  $Z$  can be determined from weak shear measurements alone, without the need to infer  $\kappa$  or to resolve the mass sheet degeneracy.

Thus, given the X-ray and weak lensing observations, the hydrostatic equilibrium condition, the cosmology and the distribution of source redshifts, we can infer the elongation,  $Z$ . This breaks the degeneracy. Recalling that the X-ray and SZ effect observations determine  $DZ$ , we see that we can infer  $D$  and thus  $H_0$ .

### 3. Cluster De-projection

Finding the three-dimensional cluster properties from the two-dimensional observations is an inverse problem. Following the usual approach, we construct a set of parameterized three-dimensional cluster models. The angular diameter distance to the cluster is included as one of the parameters. For any given set of parameter values, we can predict the observations from the model. We define a  $\chi^2$  function quantifying the differences between the actual observations and these predictions, and minimize it to find the best fit parameters.

As always, the trick is to choose the set of models well. If the set is not general enough, we will get deceptively tight constraints on the distance, based as much on the restricted

choice of models as on the data. Any systematic differences between the best-fitting model and the data may also translate into systematic errors in our estimation of the distance and elongation. On the other hand, if the set is too general, it will be impossible to constrain the parameters.

To begin, we will discuss the appropriate symmetry assumptions for elongated clusters in §3.1. We will argue that an ellipsoidal mass distribution is the best choice. In §3.2, we will discuss the constraints on the mass distribution from the weak gravitational lensing observations. We will then add a hydrostatic equilibrium model for the gas and define the  $\chi^2$  function in §3.3

### 3.1. De-projection and Symmetry

Projection always involves loss of information. Therefore, de-projection requires symmetry assumptions. Since we are interested in elongated clusters, it is natural to consider ellipsoidal symmetry. Analytically, the de-projection is simplest if the gas properties, and thus the gravitational potential, are constant on a family of similar, concentric, coaxial ellipsoids. Unfortunately, there is no guarantee that a given ellipsoidal potential will correspond to a physically sensible mass density distribution,  $\rho = \nabla^2\phi/4\pi G$ . In particular, for isothermal gas, the ellipsoidal generalization of the usual  $\beta$ -model for cluster X-ray emissivity has a potential

$$\phi \propto kT \log(1 + m^2). \quad (15)$$

However, for prolate ellipsoids with axis ratio greater than  $\sqrt{3}/2$ , the corresponding density distribution becomes dumbbell-shaped, which is unlikely for a cluster in equilibrium. For oblate ellipsoids with axis ratio less than  $\sqrt{1}/2$ , the density actually becomes negative in some regions. Thus, while the ellipsoidal potential model was useful for demonstrating the distance-elongation degeneracy and its resolution analytically in §2, it is not necessarily the best model to use in practice.

Therefore, we will instead assume that the total mass density is constant on similar ellipsoids. This ensures a sensible mass distribution. However, it also means that the isopotentials will not in general be ellipsoids. In addition, the shapes of the isopotentials will depend not only on the shape of the isodensity contours, but on the density profile,  $\rho(m^2)$ , as well. Thus, we cannot construct a model to predict the X-ray and SZ effect observations until we have determined the density profile. Consequently, we must break the construction of the model into two steps. First, we construct a set of possible mass models, including both the shape and the density profile, as constrained by the gravitational lensing observations. For each mass model, we calculate the gravitational potential. Second, we add the

intracluster gas in hydrostatic equilibrium. This allows us to predict the X-ray and SZ effect observations, and to adjust the free parameters of both the mass and gas models to find the best fit.

Jing & Suto (2002) have fit triaxial models to the mass within isodensity contours of simulated clusters. They find that the orientation of the axes is relatively stable as a function of density, though the central regions tend to be more elongated. However, to keep the number of model parameters to a minimum, we use ellipsoids of fixed shape and orientation.

### 3.2. Gravitational Lensing and the Mass Model

The shape of a triaxial ellipsoidal mass distribution is described by a pair of axis ratios. The orientation relative to the observer’s line of sight is specified by three Euler angles. These five parameters, together with the density profile,  $\rho(m^2)$ , characterize the mass distribution. There is an additional arbitrary choice of scale in the definition of  $m^2$ . However, a re-scaling of  $\rho(m^2)$  can always compensate for a change in the choice of scale, so the scale is not an additional parameter.

The weak gravitational lensing observations measure the convergence,  $\kappa(\boldsymbol{\theta}) = \Sigma(\boldsymbol{\theta})/\Sigma_{\text{cr}}$ . The critical surface density depends on  $H_0$ , but the product  $D_l\Sigma_{\text{cr}}$  does not. Thus, we can measure the product

$$D_l\Sigma(\boldsymbol{\theta}) = D_l \int dl \rho. \quad (16)$$

For an ellipsoidal mass distribution,  $\rho(m^2)$ , the projected mass density will be constant on a family of similar ellipses, parameterized by a single axis ratio and a single orientation angle. By fitting an elliptical projected mass distribution to the lensing data, we obtain these two parameters, together with  $D_l\Sigma$  as a function of the elliptical coordinate,  $b$ , defined analogously to the ellipsoidal “radius”,  $m$ . Uncertainties in the lensing data will of course allow for some variation in these quantities. For now, however, we will assume that they are fixed.

Since the shape and orientation of the ellipsoidal distribution are described by five parameters, there will still be three free parameters required to uniquely determine the shape and orientation of the mass distribution, even with perfect lensing information. First, consider a particular member of this three-dimensional parameter space; suppose that the surfaces of constant density are prolate axisymmetric ellipsoids generated by rotating the elliptical contours of projected mass about their major axis. Then, we can de-project to find

the density profile  $D_l^2 \rho(m^2)$  in the same way one de-projects a spherical distribution.

To obtain the rest of the possible ellipsoidal de-projections, we consider the three families of transformations which map ellipsoids into ellipsoids without changing the projected mass distribution. Specifically, one family corresponds to a stretching along the line of sight,

$$\rho(\mathbf{x}) \rightarrow \rho'(\mathbf{x}) = Z_{\text{mass}}^{-1} \rho(\mathbf{x}'), \quad (17)$$

where

$$\mathbf{x}' = (\boldsymbol{\theta}', \zeta') = (\boldsymbol{\theta}, \zeta/Z_{\text{mass}}), \quad (18)$$

and  $Z_{\text{mass}}$  is the elongation of the isodensity contours relative to the prolate case.

The other two families correspond to shear transformations,

$$\rho(\mathbf{x}) \rightarrow \rho'(\mathbf{x}) = \rho(\mathbf{x}'), \quad (19)$$

where

$$\mathbf{x}' = (\boldsymbol{\theta}', \zeta') = (\boldsymbol{\theta}, \zeta + \mathbf{s} \cdot \boldsymbol{\theta}), \quad (20)$$

characterized by a 2-vector,  $\mathbf{s}$ , in which the mass is displaced along the line of sight by an amount,  $\mathbf{s} \cdot \boldsymbol{\theta}$ , proportional to  $\boldsymbol{\theta}$ .

The stretching transformation does not commute with the shearing transformation, so we must specify the order in which they are applied. For a given elliptical projected mass distribution, we obtain a particular de-projection from the canonical prolate case by shearing it by  $\mathbf{s}$ , and then stretching it along the line of sight by  $Z_{\text{mass}}$ .

We will test various values of  $Z_{\text{mass}}$  and  $\mathbf{s}$ , and use the X-ray and SZ effect observations to determine the best values. All the projected observables are invariant under a reflection through the plane of the sky, which corresponds to  $\mathbf{s} \rightarrow -\mathbf{s}$ , so it is impossible to tell which end of the cluster is pointing at us.

Ellipsoidal clusters axisymmetric about the line of sight, for which  $\mathbf{s} = 0$ , have an axis ratio equal to  $Z_{\text{mass}}$ . In the general case of triaxial ellipsoids of arbitrary orientation, that will no longer be true. The axis ratios will depend in a complicated manner on the axis ratio of the elliptical projected mass distribution, the magnitude and orientation (with respect to the projected ellipse) of the shear,  $\mathbf{s}$ , and on  $Z_{\text{mass}}$ .

To be more precise, the shear transformation preserves the thickness,

$$\Delta\zeta(m, \boldsymbol{\theta}) = 2\sqrt{m^2 - \boldsymbol{\theta} \cdot \mathbf{S} \cdot \boldsymbol{\theta}}, \quad (21)$$

of the canonical prolate ellipsoid at fixed  $\boldsymbol{\theta}$ . However, it increases the total extent,

$$\Delta\zeta(m) \equiv \max_{\boldsymbol{\theta}} \zeta(m, \boldsymbol{\theta}) - \min_{\boldsymbol{\theta}} \zeta(m, \boldsymbol{\theta}) = 2 \max_{\boldsymbol{\theta}} \zeta(m, \boldsymbol{\theta}), \quad (22)$$

in  $\zeta$  spanned by the ellipsoid. Thus an ellipsoid with  $Z_{\text{mass}} = 1$  has the same thickness as the canonical prolate ellipsoid, but can have a much larger extent in the  $\zeta$  direction. The subsequent stretching increases both the thickness,  $\Delta\zeta(m, \theta)$ , and the extent,  $\Delta\zeta(m)$ , by a factor of  $Z_{\text{mass}}$ . Nonetheless, for lack of a better term, we will continue to refer to  $Z_{\text{mass}}$  as the line of sight elongation.

Finally, note that the isopotentials of an ellipsoidal mass distribution are rounder than the isodensity contours (and are in general not ellipsoids). Thus, even in the  $s = 0$  case, the typical elongation,  $Z$  of the isopotentials, which determines the ratio of true distance to that inferred from the spherical method, will be smaller than the axis ratio of the mass distribution. Conversely, for clusters in hydrostatic equilibrium, the axis ratio of the mass distribution will be greater than the typical values estimated from the shapes of X-ray isophotes.

The calculation of the potential of an ellipsoidal mass distribution has been extensively discussed (see, e.g., Chandrasekhar 1987; Binney & Tremaine 1987). Since we are working in coordinates in radians,

$$\nabla_{\mathbf{x}}^2 \phi(\mathbf{x}) = D_l^2 \nabla_{\mathbf{r}}^2 \Phi(\mathbf{r}) = 4\pi G \rho(\mathbf{x}) D_l^2 \quad (23)$$

so the potential,  $\phi(\mathbf{x})$ , is defined in terms of the combination  $\rho(\mathbf{x}) D_l^2$  which is determined by the observations, independent of  $H_0$ . It is convenient to choose the zero point of the potential at the center of the cluster. Note that the hydrostatic equilibrium condition, equation (4), has the same form in terms of the dimensionless  $\mathbf{x}$ , as long as the pressure is also differentiated with respect to  $\mathbf{x}$ .

### 3.3. Gas Model and the Chi-Squared Function

Once we have the cluster potential,  $\phi(\mathbf{x})$ , we can add the intracluster gas. In hydrostatic equilibrium, the gas can be described by its temperature profile,  $T(\phi)$  and the central electron density,  $n_{e0}$ . To minimize  $\chi^2$  numerically, we need a discrete parameterization for the temperature profile. We let  $\log T(\phi)$  be a polynomial of fixed order in  $\phi$ .

We then integrate equation (10) to obtain the density profile,  $n_e(\phi)$ . From the density and temperature profiles, we can calculate the electron pressure and X-ray emissivity in each energy band. Using  $\phi(\mathbf{x})$ , and including a factor of  $D$  for the path length, we can project to predict the SZ effect temperature decrement and the X-ray surface brightness. Given a model of the instruments used to observe the cluster, we can convert these predictions to the measured quantities.

The predictions depend on the various parameters of the model. They depend nonlinearly on the elongation and shear,  $Z_{\text{mass}}$  and  $\mathbf{s}$ , which fix the shape and normalization of the deprojected mass distribution, as well as on the central electron density,  $n_{e0}$ , and the temperature profile,  $T(\phi)$ . Finally, they are proportional to the angular diameter distance,  $D$ , to the cluster.

We construct a  $\chi^2$  function for the X-ray and SZ effect measurements in the usual way, weighting the square of the differences between the observations and the model predictions by the reciprocal of the variance of each measurement. We apply the chain rule to calculate the partial derivatives of  $\chi^2$  with respect to the gas parameters and the distance. The dependence on the shape of the cluster is more complicated. We therefore break the  $\chi^2$  minimization problem into an inner part and an outer part. For a fixed set of shape parameters, we minimize with respect to the gas parameters and distance to find the best fit for that shape. This minimization defines an integrated  $\chi^2$ ,

$$\chi^2(Z_{\text{mass}}, \mathbf{s}) \equiv \min_{n_{e0}, T(\phi), D} \chi^2(Z_{\text{mass}}, \mathbf{s}, n_{e0}, T(\phi), D). \quad (24)$$

Then, we minimize this integrated  $\chi^2$  with respect to the elongation and shear,  $Z_{\text{mass}}$  and  $\mathbf{s}$ , which determine the shape of the cluster. For the inner minimization with respect to the gas parameters and distance, we use the Levenberg-Marquardt nonlinear chi-squared minimization algorithm, which takes advantage of the derivative information.

Note that the lensing observations are not included in the  $\chi^2$  function. We already had to use them to fix the projected mass density, and thus determine  $\phi$ , up to the three remaining shape parameters. Without this, we could not have made predictions for the projected gas observables. This special role for the lensing data is a direct consequence of our choice of symmetry assumption for the mass distribution; the shape of the isopotentials contours depends on the mass profile, and not just on the shape of the mass distribution.

As a result, the effect of uncertainties in the lensing observations must be considered separately. They will lead to some range of acceptable parameters in the fit to the projected mass information in §3.2. By repeating the inversion procedure for different values of these parameters, we can test the effect on the angular diameter distance.

#### 4. Test Cases

To test our de-projection method, we apply it to artificial observations of model clusters, to see how well we recover the original shape and distance. We will refer to these clusters as the true clusters. Our true clusters, like the models used to fit them, have ellipsoidal

mass distributions, so that we know a priori what the best fit shape ought to be in the absence of noise. The purpose of this test is to determine how sensitive the method is to the uncertainties in the observations. In particular, we want to ensure that there were no additional degeneracies which our analytic treatment in §2 might have missed.

For the mass density profile,  $\rho$ , as a function of our angular ellipsoidal coordinate,  $m$ , we use a  $\beta$ -model,

$$\rho(m) = \rho(0) \left[ 1 + \frac{m^2}{m_0^2} \right]^{-3\beta/2} \quad (25)$$

with core  $m_0$ . We choose  $\beta = 2/3$ . While such a model with a core is generally more appropriate to the X-ray gas than to the cluster matter distribution, it should be sufficient for testing purposes. This choice also reduces the number of integrals which must be done numerically to calculate the potential.

For the X-ray gas, we assume a polytropic temperature profile with a central temperature  $T = 8.0 \text{ keV}$  and a polytropic index,  $n$ , equal to 1.1. We assume a fully ionized hydrogen-helium plasma with a hydrogen fraction of 0.76 by mass. We take the central electron density,  $n_{e0}$ , equal to  $1.0 \times 10^{-2} \text{ cm}^{-3}$ . The density normalization only affects the signal-to-noise of the gas observations.

We use two sets of true clusters. First, we consider ellipsoidal clusters axisymmetric about the line of sight, which we fit with models with the same symmetry. This allows us to treat the observables as functions of one variable, the angular radius,  $\theta$ . It also reduces the shape parameter space from three dimensions to one, the mass elongation,  $Z_{\text{mass}}$  relative to spherical. Both changes greatly reduce the CPU time required for the inversion. We consider clusters with different elongations,  $Z_{\text{mass}}$ , in the mass distribution, relative to spherical, ranging from 0.6 to 1.4. We normalize each density profile to produce the same projected mass, regardless of the elongation. Thus, we are testing whether the X-ray and SZ effect measurements allow us to distinguish between clusters with identical lensing observations. Recall that the elongation,  $Z$ , of the potential, which directly affects the inferred distance, is generally smaller than  $Z_{\text{mass}}$ .

Second, we consider the more general case of clusters of arbitrary shape and orientation. For this case, we use three true clusters: two triaxial clusters and one axisymmetric but with its axis inclined to the line of sight. Their shapes are listed in Table 1. We observe the two triaxial clusters along two different lines of sight, and the axisymmetric cluster along one. Table 2 lists the trial observations. The lines of sight are specified by spherical coordinates: the inclination,  $i$ , with respect to the third ( $c$ ) axis, and the azimuthal angle,  $\phi$ , with respect to the first ( $a$ ) axis.

Table 1: Triaxial Test Cases

Shape name	Axes		
	$(h^{-1} \text{ Mpc})$		
	$a$	$b$	$c$
A	1.2	0.8	2.0
B	2.0	1.0	1.0
C	0.7	1.4	2.0

Table 2: Trial Observations of Triaxial Test Cases

Observation	Shape <sup>a</sup>	Line of sight direction	
		inclination $i^b$ (deg)	azimuthal angle $\phi^c$ (deg)
A1	A	30	40
A2	A	60	75
B	B	60	0
C1	C	30	40
C2	C	60	75

<sup>a</sup>see Table 1

<sup>b</sup>with respect to the  $c$  axis of the ellipsoid

<sup>c</sup>with respect to the  $a$  axis of the ellipsoid

When choosing the model length and density scales, it is sometimes easier to think in terms of the physical quantities. We choose the physical core length scale  $m_0 D$  to be  $0.1 h^{-1} \text{ Mpc}$ . For the clusters axisymmetric about the line of sight, we choose a central density,  $\rho(0)$ , equal to  $4 \times 10^{15} Z_{\text{mass}}^{-1} h^2 M_{\odot} / \text{Mpc}^3$ . For the other clusters,  $\rho(0) = 4 \times 10^{15} h^2 M_{\odot} / \text{Mpc}^3$ , regardless of shape and orientation.

Of course, to convert these physical quantities to the  $H_0$ -independent quantities actually used in the model, we need to specify the scaled distance,  $hD$ . We will take the redshift,  $z$ , of our clusters to be 0.2. This is far enough away to make weak lensing measurements feasible, yet close enough for X-ray instruments such as Chandra to produce high signal-to-noise maps in many energy bands. We assume a flat  $\Lambda$ CDM cosmology with  $\Omega_0 = 0.3$  and  $\Lambda_0 = 0.7$ , which gives  $D = 476 h^{-1} \text{ Mpc}$ . Then, we calculate  $m_0$  and  $\rho(0)D^2$ .

Note that for a given choice of the physical quantities, the angular scale of the cluster, will vary slightly with cosmology, as will the normalizations of the X-ray and SZ effect observations. Thus, the signal-to-noise of these observations does depend slightly on our

choice of cosmology. However, the angular scale and signal-to-noise would also vary from cluster to cluster in a given cosmology. In a different cosmology, the same calculation with the same angular scale and signal-to-noise would simply correspond to a slightly different physical cluster, but would not be fundamentally altered.

When we project the local electron pressure and X-ray emissivity to create the artificial observations of the intracluster gas, we also need the actual distance,  $D$ . We take  $h = 0.7$ , so  $D = 681$  Mpc. Again, given the choice of the physical mass profile parameters, this will affect the signal-to-noise. Of course, neither this assumed value of  $h$  nor that of  $D$  is used by the de-projection procedure.

## 5. Artificial Observations

Next, we need to create artificial observations of these cluster models, both the true clusters and the trial models used in the  $\chi^2$  fitting. Our goal is to see how the observational noise and uncertainties affect our ability to recover the true shape and distance. We do not attempt to model in detail all of the properties of specific instruments. Instead, we use simplified models with roughly the same sensitivity. The possibility of creating high signal-to-noise weak lensing and SZ effect maps is relatively new. Therefore, we allow for some improvement over the current state-of-the-art in these observations. The field of X-ray astronomy is comparatively mature, so we base our model more closely on current instrumentation. We add noise to the true cluster observations but not to the trial models. Otherwise, we use the same models to create both sets of artificial observations.

### 5.1. Weak Lensing

As we mentioned in §3.3, incorporating uncertainties in the weak gravitational lensing measurements requires additional Monte Carlo testing of the entire de-projection analysis. Because of this, as well as rapid advances in the weak lensing observations, we have entirely ignored the weak lensing uncertainties in our initial tests. Instead, we use the exact de-projection of the density profile of the true cluster. In doing so, we are also not restricting ourselves to using only the weak shear information. Thus, while we showed in §2.4 that the elongation could be recovered from the weak shear alone, our numerical tests do not demonstrate this.

## 5.2. SZ Effect

We base our artificial SZ effect observations roughly on the maps made by fitting the Owens Valley Radio Observatory (OVRO) millimeter-wave interferometer with 30 GHz (1 cm wavelength) receivers (Carlstrom, Joy, & Grego 1996). At this frequency, the proportionality constant between the temperature decrement and the Compton  $y$ -parameter in equation (2) differs slightly from  $-2$ . Relativistic corrections (Rephaeli 1995; Challinor & Lasenby 1998) also modify the proportionality constant. However, the total correction is roughly 5% (Patel et al. 2000), so we ignore it.

A two-element interferometer measures the complex visibility,

$$V(\mathbf{u}) = \int d\boldsymbol{\theta} I(\boldsymbol{\theta}) \exp(-2\pi i \mathbf{u} \cdot \boldsymbol{\theta}), \quad (26)$$

a Fourier component of the intensity,  $I$ , where  $\mathbf{u} = \Delta\mathbf{r}/\lambda$  is the baseline separation of the antenna elements in units of the wavelength,  $\lambda$ . Equation (26) is valid as long as the separation,  $\Delta\mathbf{r}$ , between the antennas is much larger than their diameter, which is usually the case in radio interferometry. The Fourier transform of this sparse Fourier-space sampling is called the “dirty” beam. Taking the Fourier transform of the visibilities results in a “dirty” image which is the convolution of the true intensity with the dirty beam. Convolution techniques are used to recover a smooth, “clean” image with the equivalent resolution. Clusters of galaxies, however, are large compared to the angular resolution of interferometric arrays. The ability to measure the temperature decrement on large scales is limited by the shortest baselines. Therefore, these observations are generally made with the array in a nearly close-packed configuration to maximize sensitivity to the SZ temperature decrement on cluster scales, with some longer baselines for detection and removal of point sources. For OVRO, this system produces a roughly  $1'$  beam and maps with an rms noise of  $\sim 27 \mu\text{K}$  per beam in the temperature decrement with 60 hr of observations (Patel et al. 2000). We adopt this resolution and sensitivity.

Such close-packed configurations produce “dirty” beams which are actually smooth, so the data can be analyzed in real space (Pen et al. 2002). The temperature decrement measurements have Gaussian white noise, so the noise remains uniform and Gaussian when transformed to real space. The physical separation of the dishes must be greater than the diameter of the individual dishes. This limits the shortest baselines measured, which results in a hole in the Fourier space coverage. In real space, the effect of this hole is approximately equivalent to subtracting the diffraction limited image which would be produced by a single dish from an image with the diffraction limit of the entire array. This gives an effective beam which has a total area of zero, as appropriate for interferometric observations with

no measurements at zero-spacing. For the OVRO array, each dish has a 10.4 m diameter, corresponding to a diffraction limit of 4' at 30 GHz.

For simplicity, in the axisymmetric case, we limit the field of view of our temperature decrement observations to 3' in radius, covered with three 1' annuli, and remove the short baselines by subtracting the average temperature decrement over this field from the individual annuli. This simple approach produces the correct spatial resolution and noise per pixel, but it reduces the field of view and the total number of pixels. It also ties the diameter of the field of view to the dish size, preventing us from changing one without changing the other.

For clusters with arbitrary orientation, the field of view is no longer circular, so this approach no longer makes sense. Therefore, we use an  $8' \times 8'$  field of view, with a rectangular grid of 1' pixels, to represent the image with the diffraction limit of the entire array. We then convolve this image with a Gaussian of unit area and full width at half maximum equal to the single dish diffraction limit and subtract the convolved image from the original.

### 5.3. X-ray Observations

For our artificial X-ray observations, we use a simplified model of the Advanced CCD Imaging Spectrometer (ACIS) on the Chandra X-ray Observatory as described by the Chandra Proposers' Observatory Guide (2001). The four front-illuminated CCD chips of the ACIS-I imaging configuration have  $0.492''$  pixels over a  $16.9' \times 16.9'$  field of view. The half-energy radius varies roughly from 1 to 10 pixels from the center of the field of view to an off-axis angle of 8'. The full spatial resolution is unnecessary for our purposes, so in the axisymmetric case, we use 50 annuli, each  $9.6''$  wide, out to a radius of 8'. In the case of the clusters of arbitrary orientation, we use a  $20^2$  rectangular grid covering an  $8' \times 8'$  field of view (one-quarter of the Chandra ACIS-I field), giving  $24'' \times 24''$  pixels. This resolution is quite crude, but is necessary to ensure that the chi-squared fitting can be performed in a reasonable amount of CPU time.

For simplicity, we ignore X-ray line emission and consider only thermal Bremsstrahlung. The ACIS energy resolution varies with energy and position on the chips. However it is generally  $\lesssim 0.3$  keV. We create maps in 30 energy bands of this width between 1 keV and 10 keV. To calculate the count rates, we multiply the X-ray surface brightness for each band by the angular area of each annulus and by the effective area of each band. We assume an effective area of  $A = 500 \text{ cm}^2$  for  $E < 2 \text{ keV}$ ,  $300 \text{ cm}^2$  for  $2 < E < 5.5 \text{ keV}$ , and a linear falloff in  $\log A$  to  $14.3 \text{ cm}^2$  from 5.5 keV to 10 keV. This approximates the on-axis effective area of the front-illuminated CCDs, while simplifying the detailed edge structure. For simplicity, we

also ignore the change in effective area with off-axis angle, which is roughly a 15% decrease at the edge of our field of view.

We add a contribution to the count rates from the background (both the actual diffuse X-ray background and the charged particle background) of 0.07 counts/chip/sec for  $E < 2\text{ keV}$  and 0.15 counts/chip/sec for energies from 2 keV to 10 keV as estimated from the on-orbit measured background for the ACIS-I chips (Chandra Proposers' Observatory Guide 2001). For simplicity, we add the same background to the count rates for the trial models, rather than adding a background term whose normalization is a free parameter of the fit.

We multiply the count rates by an assumed 100 ksec observation time to find the expected number of counts in each band and annulus, and add Poisson fluctuations to these counts. Note that when we compute the Poisson uncertainties in the number of counts for the  $\chi^2$  function, we use the mean values. With actual observations, only the measured number of counts including noise would be known. This would introduce a bias to actual observations, which would have to be corrected.

## 6. Numerical Details

The projected gas observables, the X-ray surface brightness and the temperature decrement, are approximated by discrete sums as described in the Appendix.

Our true clusters have ellipsoidal mass distributions, so the projected mass distributions are elliptical. Since we are not including any uncertainties in the lensing information, it is not necessary to fit an elliptical model to the projected mass and de-project it explicitly for each assumed shape. The de-projected mass profile will differ from the true profile,  $\rho(m^2)$ , only by the ratio of the true mass elongation,  $Z_{\text{mass}}$ , to the assumed value.

For clusters axisymmetric about the line of sight, our shape parameter space is reduced to a single dimension, the elongation,  $Z_{\text{mass}}$ . For simplicity, we perform the outer minimization of  $\chi^2$  with respect to elongation by a simple grid search. We evaluate the integrated  $\chi^2(Z_{\text{mass}})$  on a uniform grid of 33 values of assumed elongation in a range of  $\pm 0.2$  about the true elongation, and pick the elongation which gives the lowest chi-squared.

In the case of clusters of arbitrary shape and orientation, such a brute force grid search is no longer feasible. Instead, we use a general-purpose multidimensional minimization routine based on Powell's method. To ensure that the minimization routine has converged, we restart it twice at the previous minimum. In practice, there was no significant change in the solution after the first restart.

To find the initial guess for this minimization routine, we perform a low resolution grid search over a 4 by 2 by 2 grid of cells. We initially evaluate the integrated  $\chi^2$  at the center of each cell and find the cell with the smallest value. We then refine the grid by evaluating  $\chi^2$  in a 3 by 3 by 3 grid within this cell. The shape with the smallest integrated  $\chi^2$  is used as the initial guess for the minimization routine.

As mentioned earlier, we need a discrete parameterization for the temperature profile. We take  $\log T(\phi)$  be a polynomial of fixed order in  $\phi$ . in the axisymmetric case, we used a fourth order polynomial. In the general case, we found that a third order polynomial was more effective in avoiding unphysical oscillations in the temperature profile in the initial guess for the cluster shape was poor.

The inner minimization, with respect to the gas parameters and the distance, also requires an initial guess. We guess a constant temperature profile of 7.7 keV, roughly equal to the true central temperature of 8 keV. In the axisymmetric case, we take the central electron density to be twice the true value, and the distance to be  $0.833Z_{\text{mass}}^{-1}$  (assumed) of the true value. In the general case, we take the central density to be 1.5 times the true value, and the distance to be 1.1 times the true value. As long as the initial guess for the temperature is not too extreme, the code rapidly converges to essentially the same best fit set of parameters, regardless of the choice of initial guess. Using a fairly accurate initial guess for the central temperature is realistic since the central temperature of a relaxed cluster should be reasonably well determined from the overall emission-weighted spectrum.

For each test case, we create 20 realizations of the artificial observations with noise, which are analyzed independently. This allows us to estimate the uncertainties in the parameters inferred from a single observation due to statistical uncertainties in the measurements.

## 7. Results

### 7.1. Axisymmetric Clusters

First, we show the results of fitting the true clusters which are axisymmetric about the line of sight, with models of the same symmetry. Figure 1 shows the mean values of the inferred mass elongation for each true elongation. The error bars are the  $1\sigma$  uncertainties for a single realization, calculated from the sample variance of the 20 realizations. The diagonal line shows  $Z_{\text{mass}}(\text{inferred}) = Z_{\text{mass}}(\text{true})$ . The mean elongations are consistent with no bias relative to the true elongations (with a  $3\sigma$  upper limit of 1 to 2%). The uncertainties for a single realization range from 1 to 3%. Since we plot mean values (to test for systematic bias), the deviations from the true elongation are of course much smaller than the error bars,

which represent the uncertainty in a single realization.

The inferred elongations shown are from simultaneous fits for the elongation, distance, central density, and temperature profile. However, we obtain nearly identical results if we use only the X-ray and lensing data, and fit for elongation, temperature profile, and the combination  $n_{e0}^2 D$ . This is to be expected from our analytic analysis in §2.4, where we saw that constraining elongation required the absolute temperature and the relative temperature and density profiles. The SZ effect by itself only constrains the product of the two profiles. Nor can it constrain the absolute temperature, if  $H_0$  and thus the cluster distance are unknown. Therefore, the elongation is likely to remain determined primarily by the X-ray and lensing observations, even with improvements in the temperature decrement measurements.

In Figure 2, we show the inferred distance for clusters of each true elongation. Again, the values and error bars represent the mean over the 20 realizations, and the  $1\sigma$  uncertainties of a single realization. The dashed line indicates the true distance of 681 Mpc. There is no significant bias (with a  $3\sigma$  upper limit of 1 to 2%), and the uncertainties in a single realization are of order 2 to 3%.

## 7.2. General Case

Next, we fit triaxial models to the second set of true clusters described in §4, those with arbitrary orientation and shape. For each observation listed in Table 2, we created 20 realizations of the noise, and analyzed each one independently. Figure 3 shows the inferred angular diameter distance for each observation. The values represent the mean of the 20 realizations. The error bars are the  $1\sigma$  uncertainties due to instrumental noise for a single realization, calculated from the sample variance, which range from 3 to 6%. The dashed line indicates the true distance of 681 Mpc. The mean distances are consistent with no bias, with  $3\sigma$  upper limits ranging from 2 to 4%.

The true elongation,  $Z_{\text{mass}}$  is recovered to 2 to 4%. The absolute errors in the shear ranged from 0.05 to 0.10.

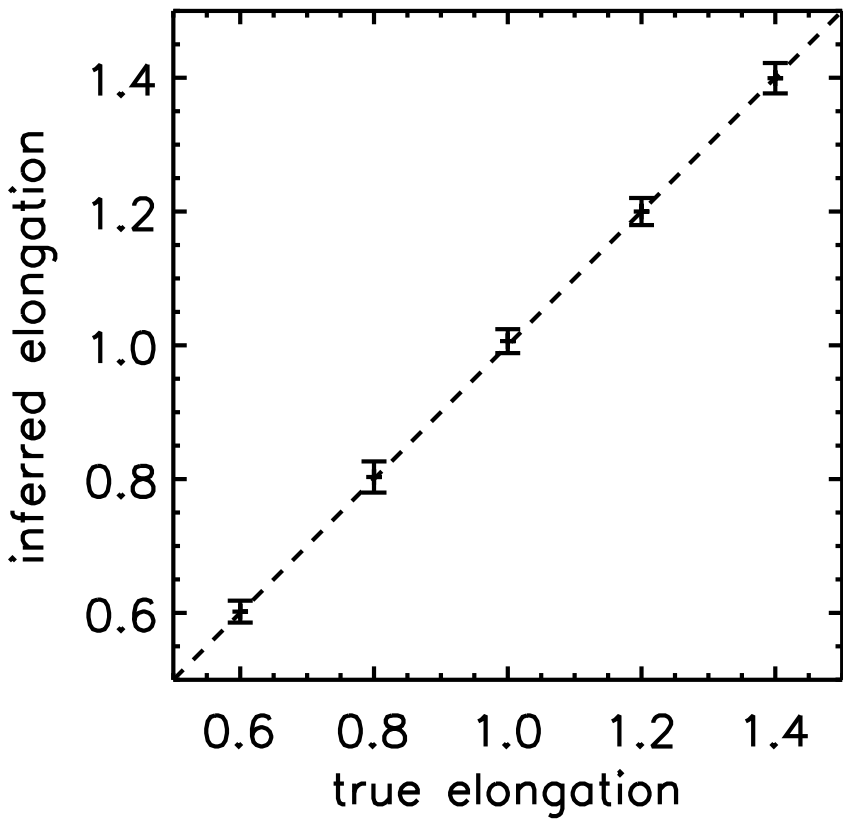


Fig. 1.— Inferred vs. true mass elongation,  $Z_{\text{mass}}$ , as estimated from 20 realizations of the artificial observations. The error bars are the sample standard deviation of the 20 realizations, corresponding to the  $1\sigma$  uncertainties for a single realization.

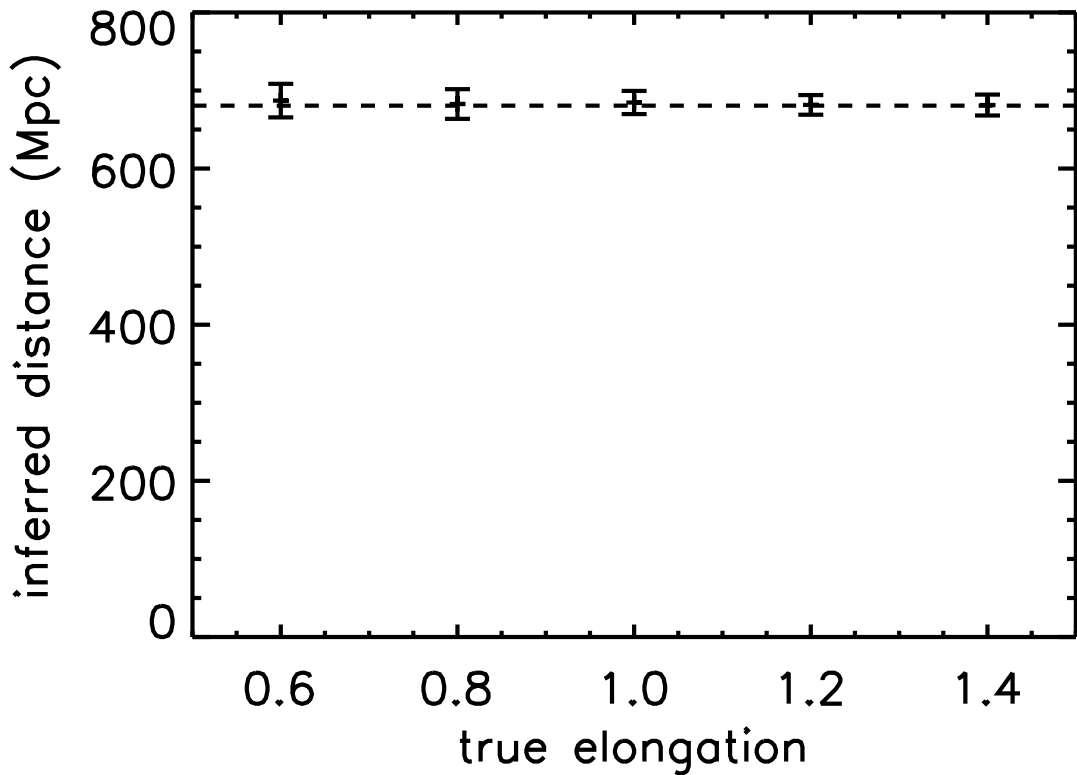


Fig. 2.— Inferred distance for each true mass elongation,  $Z_{\text{mass}}$  as estimated from 20 realizations of the artificial observations. The error bars are the sample standard deviation of the 20 realizations, corresponding to the  $1\sigma$  uncertainties for a single realization.

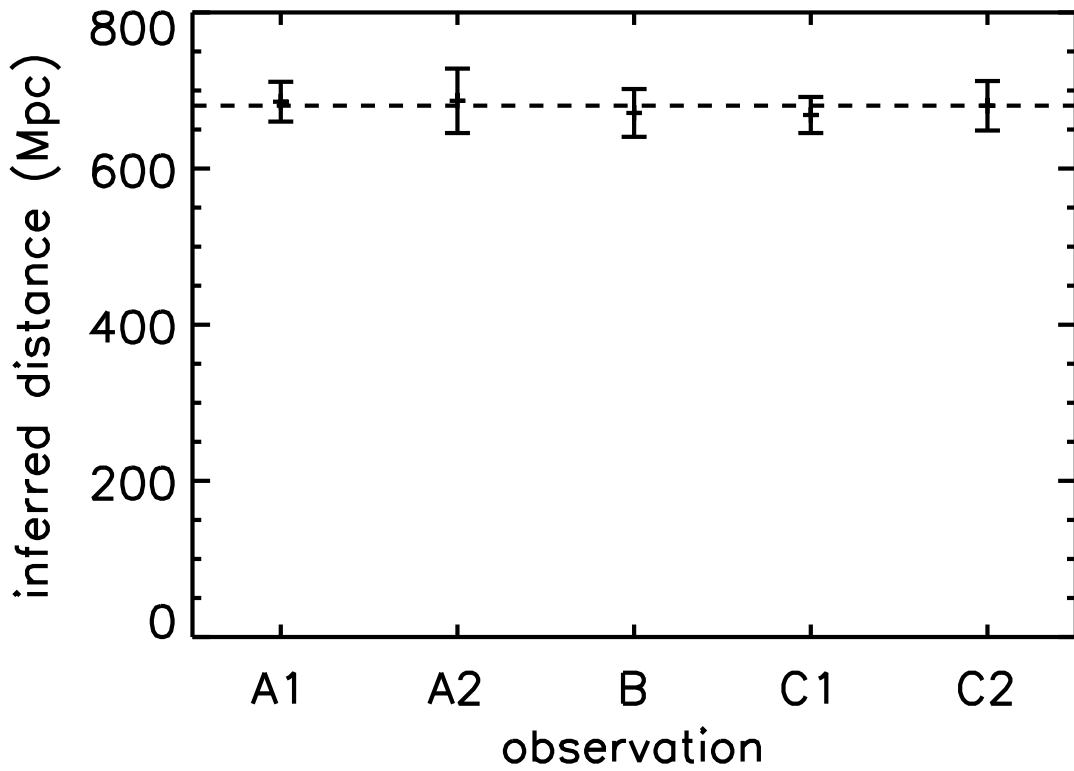


Fig. 3.— Inferred distance for each trial observation (see Table 2) as estimated from 5 realizations of the artificial observations. The error bars are the sample standard deviation of the 5 realizations, corresponding to the  $1\sigma$  uncertainties for a single realization.

## 8. Discussion

### 8.1. Statistical Uncertainties

The variation among realizations measures the sensitivity of the inferred distance to statistical uncertainties in the X-ray and temperature decrement observations. By examining correlations between the fractional errors in the distance and in the mass elongation, it is possible to show that the uncertainty in the X-ray temperature makes the dominant contribution to the uncertainty in the distance in the case of clusters axisymmetric about line of sight (Fox 2001). In the general case, however there was no obvious correlations between the distance and the shape parameters,  $Z_{\text{mass}}$  and  $\mathbf{s}$ .

As we noted in §5.1, we have not attempted to model the uncertainties in the gravitational lensing observations. Additional Monte Carlo tests with realistic treatment of these uncertainties, and their effects on the fitting and de-projection of the surface mass distribution, should be performed.

### 8.2. Systematic Errors

Besides the statistical measurement uncertainties, there are number of systematic effects which could affect our determination of the cluster distances and of  $H_0$ . Many of these effects are also relevant to the traditional method based on a spherical model. For recent reviews of the systematic uncertainties, see Carlstrom et al. (2001) and Molnar, Birkinshaw, & Mushotzky (2002).

We will focus primarily on those effects which are particular to our method. We first discuss the dependence of the inferred  $H_0$  on the magnitude of the observed quantities, and the resulting bias due to either contamination of these observations or to errors in their absolute calibration. Then, we consider aspects of the state of the intracluster gas which could violate the underlying physical assumptions of our model. Finally, we mention some caveats regarding our assumption of ellipsoidal symmetry.

#### 8.2.1. Normalization Dependence

The distance determination depends on the normalizations of the measured temperature decrement, X-ray surface brightness, and X-ray temperature. Therefore, calibration errors or other systematic errors in these observations will directly affect the value of  $H_0$  inferred.

In the traditional method,

$$H_0 \propto D_{\text{inferred}}^{-1} \propto \frac{\Sigma_X T_e^2}{(\Delta T_{\text{CMB}})^2}, \quad (27)$$

assuming that the value for  $H_0$  has been averaged over sufficiently many clusters of random orientation to remove the effect of the elongation. For a single cluster, there would be an additional factor of the inverse of the gas elongation,  $Z$ . In our method,  $H_0$  can, in principle, be inferred from a single cluster by correcting for this factor. However, this correction introduces an additional dependence on the ratio of the potential,  $\phi$ , determined from weak lensing observations, to the X-ray temperature. From equations (13) and (14), we can show that the inferred gas elongation,

$$Z \propto \frac{\Sigma_{\text{cr}} D_l \psi}{T_e}. \quad (28)$$

Recall that the product  $\Sigma_{\text{cr}} D_l$  is independent of the distance to the lensing cluster,  $D_l$ , and depends only on the cosmology and the redshifts of the cluster and the lensed sources. Combining equations (27) and (28), we see that for our method,

$$H_0 \propto D_{\text{inferred}}^{-1} \propto \frac{\Sigma_{\text{cr}} D_l \psi \Sigma_X T_e}{(\Delta T_{\text{CMB}})^2}. \quad (29)$$

Thus, our method and the traditional method have the same sensitivity to errors in the normalization of the X-ray surface brightness or the temperature decrement. Possible sources of contamination of these measurements, as well as uncertainties in their calibration, are discussed by Carlstrom et al. (2001).

Due to the fortuitous cancellation of one power of the electron temperature between equations (27) and (28), we expect our method to be less sensitive to the electron temperature than the traditional method. Nonetheless, the inferred value of  $H_0$  will still be directly proportional to the absolute calibration of the X-ray temperature, as well as that of the surface brightness.

Our method introduces a new dependence on the calibration of the weak lensing observations. Our inferred  $H_0$  is now proportional to the normalization of the lensing potential,  $\psi$ , (or its second derivatives, the convergence,  $\kappa$ , and the shear,  $\gamma$ ) as well as to

$$\Sigma_{\text{cr}} D_l = \frac{c^2}{4\pi G} \frac{D_s}{D_{ls}}. \quad (30)$$

For measurements of weak shear from the shapes of background galaxies, the normalization of the inferred shear depends on accurately correcting for the seeing conditions. Calculating  $\Sigma_{\text{cr}} D_l$  requires knowledge of the redshift distribution of the background galaxies, and of the choice of cosmology ( $\Omega_0$  and  $\Lambda_0$ ) which affect the shape of the redshift-distance relation. Note

that all lensing measurements depend on  $\Sigma_{\text{cr}}$ . Therefore, it may be possible to eliminate the cosmology dependence if the redshift distribution is itself inferred from lensing measurements. Several techniques have been suggested for doing so (Smail et al. 1994; Kneib et al. 1994, 1996; Bartelmann & Narayan 1995).

Our analytic models in §2 demonstrated that the elongation-distance degeneracy could be broken without resolving the mass sheet degeneracy in the lensing observations. However, while we have proven this in principle, we have not yet demonstrated it in practice. In fact, our assumption in §3.2 that the product  $D_l \Sigma$  was known presumes that the mass sheet degeneracy has been resolved. This could be done by measuring the convergence. Alternatively, we can assume that the surface density falls to negligible values far from the center of the cluster. Given shear observations over a wide enough field, this may be sufficient. Finally, the method might be reformulated to remove any dependence on the mass sheet degeneracy.

### 8.2.2. *The Physical State of the Intracluster Gas*

In comparing  $n_e^2$  inferred from the X-ray observations with  $n_e$  inferred from the temperature decrement, both our method and the traditional one assume that the X-ray emission and the scattering of the microwave background photons is due to the same population of electrons. If the intracluster gas is not smooth but rather clumpy, with  $C \equiv \langle n_e^2 \rangle / \langle n_e \rangle^2 > 1$ , then the inferred distance to the cluster will be systematically underestimated by a factor of  $C$  (Birkinshaw et al. 1991). In addition, a multiphase medium introduces additional degrees of freedom which may make it impossible to constrain the elongation. The gas in the cooling flows observed in the centers of some clusters is in fact believed to be multiphase. In applying the our method to real clusters, it would be advisable to remove any cooling flow region from the X-ray maps and fit to the remaining data.

Our method of inferring the elongation depends on the assumption that the intracluster gas is in hydrostatic equilibrium in the cluster potential well. A distinct advantage of the traditional method is that it does not rely on this assumption. The characteristic time for a cluster to reach hydrostatic equilibrium is the sound wave crossing time. The high temperature of the intracluster gas makes this time scale much shorter than the Hubble time (Sarazin 1988). However, clusters which have undergone recent mergers may not have had time to fully relax. Mergers tend to increase the X-ray luminosity of clusters, so cluster samples selected by luminosity will tend to include an enhanced fraction of mergers (Roettiger et al. 1997). Deviations from hydrostatic equilibrium could introduce either random or systematic errors in our elongation correction.

We have also implicitly assumed that thermal pressure is the dominant source of support for the gas. Other possible sources include rotation, magnetic or turbulent pressure, or pressure from a population of relativistic electrons and ions. If these were significant, our method would give incorrect results for the elongation and the distance.

It is essential to quantify these possible errors by applying the method to a set of simulated clusters.

### 8.2.3. *Symmetry and Modeling Assumptions*

Real clusters will differ from the models we use to fit them, and this may also introduce both random and systematic errors. Typically, measurements of  $H_0$  from X-ray and SZ effect observations have used a beta model to fit the gas density distribution. Often, in the absence of spatially resolved X-ray temperature measurements, an isothermal temperature has also been assumed. A number of authors have estimated the systematic effects in the traditional method due to deviations from these model assumptions, as well as that of spherical symmetry (Sulkanen 1999; Inagaki et al. 1995; Roettiger et al. 1997; Puy et al. 2000). We have tried to take advantage of the improved spectral resolution of the latest X-ray telescopes, and of anticipated improvements in observations of the SZ effect, to relax these assumptions about the density and temperature profiles of the gas, allowing them to be constrained only by the observations and by the assumption of hydrostatic equilibrium.

Even so, de-projecting clusters still requires a fairly strong assumption about symmetry. We have assumed that the cluster mass distribution is constant on families of similar, concentric, coaxial ellipsoids. Our hope is that such a model will be sufficient for inferring to first order the deviation from spherical symmetry due to elongation. However, X-ray clusters often show evidence for significant irregularity and substructure (e.g., Jones & Forman 1992; Mohr et al. 1995). If the deviations from our model are large enough, it may fail to fit the observations, or, worse, give misleading answers. For example, our model would be unlikely to give correct results when applied to a cluster which was actually two clusters along the same line of sight (unless one of the two clusters dominated all three of our observational probes, or unless the two shared a common envelope). Selection effects in the detection of gravitational lensing could bias a sample of clusters toward such cases. Even fairly regular clusters will not have the perfect ellipsoidal symmetry we have assumed. They may be elongated but not ellipsoidal. They may be roughly ellipsoidal, but with smaller scale irregularities, or with axis ratios and orientations which vary with radius. Again, the best way to quantify the resulting uncertainties, both random and systematic, is to apply the method to a sample of simulated clusters, with realistic modeling of the selection effects.

Mass in filaments and other correlated structure near clusters contributes significantly to the total projected mass measured by lensing, and to its scatter, though the magnitudes of both the bias and the scatter depend on the particular mass estimator used (Metzler et al. 1999; Metzler, White, & Loken 2001). By applying our method to numerically simulated clusters, we will be able to tell how much of an effect this has on the inferred distances.

## 9. Conclusions

X-ray and SZ effect observations provide a geometric method of measuring the distance to clusters of galaxies, independent of the usual distance ladder calibrations. This method can be used to measure the redshift-distance relation and inferred the value of  $H_0$ . However, the method is subject to an exact degeneracy between the distance and the elongation of the cluster along the line of sight, relative to its size perpendicular to the line of sight. This degeneracy introduces significant scatter in the measured values of  $H_0$ , requiring a large sample of clusters of random orientation for an accurate determination. To infer  $\Omega_0$  and  $\Lambda_0$  by the redshift-distance relation would require an even larger sample. Furthermore, if the sample is biased towards particular orientations due to selection effects, this would introduce a systematic error in  $H_0$ .

The elongation-distance degeneracy can be broken if the intracluster gas is in hydrostatic equilibrium, and if the projected mass density can be inferred from gravitational lensing measurements of background galaxies. We have developed a specific method to do so, using models with ellipsoidal mass distributions, and applied it to simple axisymmetric ellipsoidal model clusters. We recover the true shape and distance to each cluster with statistical uncertainties of 4 to 6%, and no detectable systematic bias (with a  $3\sigma$  upper limit of 4%), using artificial X-ray and SZ effect observations with sensitivity comparable to current observations.

Further work is necessary to determine the sensitivity of the method to realistic uncertainties in the lensing observations. Particular attention should be paid to possible systematic uncertainties due to the mass sheet degeneracy, and to the dependence of the critical surface density on the redshift distribution of the lensed background galaxies. The systematic uncertainties in the calibration of the X-ray surface brightness and temperature observations and the SZ effect observations are also important.

Finally, real clusters are not the perfectly regular, ellipsoidal objects we have assumed in our models, nor are they necessarily in perfect hydrostatic equilibrium. It is essential to test the method by applying it to numerically simulated clusters, which more closely resemble

real clusters, at least in their greater degree of messiness.

We would like to thank Abraham Loeb for suggesting combining X-ray and lensing observations to infer the line of sight elongation of clusters, and for his advice on an earlier incarnation of this project. This work was supported by a National Science Foundation Graduate Research Fellowship for D. C. F.. Many thanks to Laura Grego and Chris Metzler for useful discussions, and to Irwin Shapiro for pulling at a loose thread in the preliminary results. One of the authors (D. C. F.) would like to acknowledge Dragon Systems, Inc., whose DragonDictate for Windows and Dragon NaturallySpeaking software were essential to the development of the code for this calculation and to the preparation of this paper.

## A. APPENDIX

Since the gas properties are constant on isopotentials, the projection of a local gas quantity,  $f(\phi)$ , is

$$\Sigma(\boldsymbol{\theta}) = D \int d\zeta f(\phi(\boldsymbol{\theta}, \zeta)). \quad (\text{A1})$$

The projection operator is linear, and we already have a finite set of  $n$  lines of sight,  $\boldsymbol{\theta}_i$ , so an obvious approach is to discretize the local quantity, and calculate a projection matrix,  $K$ . We pick a finite grid in  $\phi$ ,  $\phi_0 < \phi_1 < \dots < \phi_{m-1} \equiv \phi_{\max}$ . Then, the projection reduces to a matrix-vector multiplication,

$$\Sigma(\boldsymbol{\theta}_i) = \sum_j D K_{ij} f_j \quad (\text{A2})$$

where  $f_j \equiv f(\phi_j)$ . Similarly, the gradient with respect to the gas parameters,  $\mathbf{a}$ , is simply a matrix-matrix multiplication,

$$\nabla_{\mathbf{a}} \Sigma(\boldsymbol{\theta}_i) = \sum_j D K_{ij} \nabla_{\mathbf{a}} f_j \quad (\text{A3})$$

To calculate the elements of the projection matrix,  $K$ , we replace  $f(\phi)$  in equation (A1) with a linear interpolation in  $\phi$  between the grid points. When  $\phi < \phi_0$ , we let  $f(\phi) \equiv f(\phi_0)$ . For each line of sight, we cut off the integral at  $\phi = \phi_{\max}$ . The elements of  $K$ , depend only on the potential,  $\phi(\mathbf{x})$ , the potential grid, and the set of lines of sight, not on the local gas properties,  $f$  (or  $\nabla_{\mathbf{a}} f$ ). Thus, we can use the same matrix for all X-ray bands, and for all trials with a single assumed cluster shape.

The correct choice of the cutoff,  $\phi_{\max}$ , is rather delicate. Because it is proportional to the electron density squared, the X-ray emission along a given line of sight is dominated by

the contribution from isopotentials near the minimum of  $\phi(\theta, \zeta)$  with respect to  $\zeta$ . If  $\phi_{\max}$  is too large, none of the lines of sight will have a minimum potential comparable to it. In that case, the gas properties at that isopotential will be poorly constrained, and minimizing  $\chi^2$  may lead to an unphysical temperature profile. On the other hand, if  $\phi_{\max}$  is too small, the cluster emission will be artificially cut off at some radius within the field of view. This radius may not be the same for both the model cluster and the true cluster, which will lead to systematic problems in the fitting. In addition, fixing  $\phi_{\max}$  to a single value for all models tends to bias the shape fitting. More elongated de-projections have shallower potential wells, so a fixed grid in  $\phi$  effectively reduces the angular resolution of these models, making their  $\chi^2$  values artificially large.

To avoid all these difficulties, we want to choose  $\phi_{\max}$  for each model shape so as to ensure that the outermost lines of sight in the field view are tangent to  $\phi = \phi_{\max}$ . In the axisymmetric case, this simply means setting  $\phi_{\max}$  equal to the minimum of the potential along a line of sight with the maximum radius. In the general case, we evaluate the minimum of the potential along the lines of sight at each corner and in the center of each edge of the field of view, and choose  $\phi_{\max}$  equal to the largest such minimum. We use a uniform grid in the potential with 20 elements between 0 and  $\phi_{\max}$ .

## REFERENCES

Bartelmann, M., & Narayan, R. 1995, ApJ, 451, 60

Binney, J., & Tremaine, S. 1987, Galactic Dynamics (Princeton: Princeton University Press)

Birkinshaw, M., Hughes, J. P., & Arnaud, K. A. 1991, ApJ, 379, 466

Broadhurst, T. J., Taylor, A. N., Peacock, J. A. 1995, ApJ, 438, 49

Carlstrom, J. E., Joy, M., & Grego, L. 1996, ApJ, 456, L75

Carlstrom, J. E., Joy, M., Grego, L., Holder, G., Holzapfel, W. L., LaRoque, S., Mohr, J. J., & Reese, E. D. 2001, in IAP Conf. Proc., Constructing the Universe with Clusters of Galaxies, ed. F. Durret, G. Gerbal, preprint (astro-ph/0103480)

Cavaliere, A., Danese, L., & de Zotti, G. 1977, ApJ, 217, 6

Challinor, A., & Lasenby, A. 1998, ApJ, 499, 1

Chandra Proposers' Observatory Guide, Chandra X-ray Center  
(<http://asc.harvard.edu/udocs/docs/POG/MPOG/index.html>)

Chandrasekhar, S. 1987 *Ellipsoidal Figures of Equilibrium* (New York: Dover)

Cooray, A. R. 1998, *A&A*, 339, 623

Cooray, A. R. 2000, *MNRAS*, 313, 783

Doré, O. Bouchet, F. R., Mellier, Y., & Teyssier, R. 2001, *A&A*, 375, 14

Fox, D. C. 2001, doctoral thesis (Harvard University)

Gunn, J. E. 1978, in *Observational Cosmology*, ed. A. Maeder, L. Martinet, G. Tammann (Geneva: Geneva Observatory), 1

Hughes, J. P., & Birkinshaw, M. 1998, *ApJ*, 501, 1

Inagaki, Y., Sugino, T., & Suto, Y. 1995, *PASJ*, 47, 411

Jing, Y. P., & Suto, Y. 2002, preprint (astro-ph/0202064)

Jones, C., & Forman, W. 1992, in *NATO ASI Ser. C*, 366, *Clusters and Superclusters of Galaxies*, ed. A. C. Fabian (Dordrecht: Kluwer), 49

Kaiser, N., & Squires, G. 1993, *ApJ*, 404, 441

Kneib, J.-P., Mellier, Y., Fort, B., Soucail, G., & Longaretti, P. Y. 1994, *A&A*, 286, 701

Kneib, J.-P., Ellis, R. S., Smail, I., Couch, W. J., & Sharples, R. M. 1996, *ApJ*, 471, 643

Mellier, Y. 1999, *ARA&A*, 37, 127

Metzler, C. A., White, M., Norman, M., & Loken, C. 1999, *ApJ*, 520, L9

Metzler, C. A., White, M., & Loken, C. 2001, *ApJ*, 547, 560

Mohr, J. J., Evrard, A. E., Fabricant, D. G., & Geller, M. J. 1995, *ApJ*, 447, 8

Molnar, S. M., Birkinshaw, M., & Mushotzky, R. F. 2002, *ApJ*, in press (astro-ph/0201223)

Patel, S. K. et al. 2000, *ApJ*, 541, 37

Pen, U.-L., Ng, K.-W., Kesteven, M., & Sault, R. 2002, preprint (<http://www.cita.utoronto.ca/~pen/download/Amiba/drift.ps.gz>)

Puy, D., Grenacher, L., Jetzer, P., & Signore, M. 2000, *A&A*, 363, 415

Reblinsky, K. 2000, *A&A*, 364, 377

Rephaeli, Y. 1995, *ApJ*, 445, 33

Roettiger, K., Stone, J. M., & Mushotzky, R. F. 1997, *ApJ*, 482, 588

Sarazin, C. 1988, X-ray Emission from Clusters of Galaxies, (Cambridge: Cambridge University Press)

Schneider, P., Ehlers, J., & Falco, E. E. 1992, Gravitational Lenses (Berlin: Springer)

Seitz, C., & Schneider, P. 1997, *A&A*, 318, 687

Silk, J., & White, S. D. M. 1978, *ApJ*, 226, L103

Smail, I., Ellis, R. S., & Fitchett, M. J. 1994, *MNRAS*, 270, 245

Sulkanen, M. E. 1999, *ApJ*, 522, 59

Sunyaev, R. A., & Zel'dovich, Ya. B. 1972, *Comments Astrophys. Space Phys.*, 4, 173

Taylor, A. N., Dye, S., Broadhurst, T. J., Benítez, N., & Van Kampen, E. 1998, *ApJ*, 501, 539

Yoshikawa, K., Itoh, M., & Suto, Y. 1998, *PASJ*, 50, 203

Zaroubi, S., Squires, G., Hoffman, Y., & Silk, J. 1998, *ApJ*, 500, L87

Zaroubi, S., Squires, G., de Gasperis, G., Evrard, A., Hoffman, Y., & Silk, J. 2001, *ApJ*, 561, 1 (in press)